Mesoscale Ocean Surface Current Structure Detected by High-Frequency Radar

LYNN K. SHAY

Division of Meteorology and Physical Oceanography, Rosenstiel School of Marine and Atmospheric Science, University of Miami, Miami, Florida

HANS C. GRABER AND DUNCAN B. ROSS

Division of Applied Marine Physics, Rosenstiel School of Marine and Atmospheric Science, University of Miami, Miami, Florida

RICKEY D. CHAPMAN

Space Oceanography Group, Applied Physics Laboratory, The Johns Hopkins University, Laurel, Maryland

(Manuscript received 1 July 1994, in final form 10 February 1995)

ABSTRACT

The quality and vertical correlation scales of high-frequency (HF) radar-derived ocean surface current measurements from an ocean surface current radar (OSCR) are assessed by comparing surface to subsurface current observations from 11 June to 8 July 1993 at directional discus buoys D_W and D_E, each instrumented with a three-axis ultrasonic current meter at the 13.8- and 9.5-m depths, respectively. A dual-station OSCR mapped the current fields at 20-min intervals at a horizontal resolution of 1.2 km over a 30 km × 44 km domain inshore of the Gulf Stream using the HF (25.4 MHz) mode. Over a 27-day experimental period, surface current observations were acquired 97% of the time extending to the maximum theoretical range of 44 km. Linear regression analyses indicated a bias of 2–4 cm s^{-1} and slopes of $O(1)$. While there were periods when the daily averaged complex correlation coefficients were highly correlated (>0.8), periods of low correlation (<0.3) are explained in terms of vertical phase differences and a decoupling between surface and subsurface records.

Surface and subsurface current time series at the two mooring sites were decomposed into the tidal, mean (>48 h), near-inertial (20.7 h), and high-frequency (4.5 h) bands. Tidal analyses, based on the semidiurnal (K_2, M_2, L_2, S_2) and diurnal (K_1, O_1, P_1, Q_1) constituents, indicated maximum amplitudes of 5 cm s^{-1} at D_W, whereas these amplitudes increased offshore to a maximum of 13 cm s^{-1} at D_E. Net differences between the surface and subsurface tidal currents ranged between 2 and 5 cm s^{-1} with the largest difference of 7.7 cm s^{-1} for the K_1 constituent at D_E. The tidal currents were removed from the surface and subsurface current time series and low-pass filtered at 48 h, bandpass filtered between 18 and 23 h, and high-pass filtered at 8 h. The mean current components were highly correlated (>0.9) over most of the record with small phase differences. Intrusions of the mean flow at 3–5-day intervals were correlated with bursts of near-inertial motions having amplitudes of 20 cm s^{-1} at D_E and 15 cm s^{-1} at D_W. The frequency of these motions was shifted 5%–10% above and below f during these episodes of mean flow intrusions. The higher-frequency surface motions with amplitudes of 5–8 cm s^{-1} oscillated at periods of 4.3–4.7 h but were directly out of phase with the subsurface currents, which caused the correlations to decrease below 0.3. Thus, temporal decorrelations appeared to be a result of high-frequency motions in the internal wave band between the inertial and Nyquist (1.5 cph) frequencies.

1. Introduction

Ocean surface currents play an important role in the circulation of the world's oceans and are crucial for understanding air–sea interactions, net transport of mass in the ocean for pollution dispersion, and their contribution to earth's climate. Yet surface currents remain an elusive goal of the oceanographic community because of sampling and instrumentation issues. Given the escalating interest on the coastal ocean (Brink et al. 1992; Smith and Brink 1994), the acquisition of high quality surface current data is required for long-term monitoring of the surface circulation to study their effect on a broad spectrum of societal and environmental issues such as coastal pollution, oil spills, and mass transport.

One of the more promising techniques that has evolved over the past three decades is the high-frequency (HF) Doppler radar technique (Crombie 1955). The concept is that radio waves are backscattered from the moving ocean surface by resonant surface waves of one-half the incident radar wavelength. This Bragg scattering effect (Stewart and Joy 1974) results in two discrete peaks in the Doppler spectrum. In the absence of a surface current, the spectral peaks are symmetric and their frequency σ is offset from the

---

Corresponding author address: Dr. Lynn K. Shay, Division of Meteorology and Physical Oceanography, RSMAS, University of Miami, 4600 Rickenbacker Causeway, Miami, FL 33149-1098.

origin by an amount proportional to $2c_o\lambda^{-1}$, where c_o represents the linear phase speed of the surface wave, and λ is the radar wavelength. If there is an underlying surface current, the Bragg peaks in the Doppler spectrum are displaced by an amount of $\Delta\sigma = 2V_{cr}\lambda^{-1}$, where V_{cr} is the radial component of current along the direction of the radar. Using two radar stations, separated in space by a baseline distance of 20–30 km, it is possible to resolve the two-dimensional velocity vector.

Over the past two decades, the use of HF radio pulses to probe the ocean surface currents, such as the ocean surface current radar (OSCR), has received attention in coastal oceanographic experiments (Prandle 1987). The OSCR capabilities and specifications are listed in Table 1. Based upon the fundamental scientific concept of Bragg backscatter, the OSCR system uses an 85-m-long 16- (HF) or 32- (VHF) element phased-array antennas to achieve a narrow beam, which is electronically steered over the illuminated ocean area. The beamwidth is a function of the radar wavelength divided by the length of the phased array, which is approximately 8° for the HF mode of OSCR.

A key measurement issue has been the range of the differences from 4 to 25 cm s^{-1} between the HF-derived radar current measurements and observations by conventional techniques (i.e., current meters, drogues, etc.). Hammond et al. (1987), Prandle (1987, 1991), Osborne (1991), and Prandle and Ryder (1989) all have compared the OSCR-derived tidal components to those derived from near-surface current measurements. Since most OSCR deployments have been in regions dominated by the tides (i.e., semienclosed basins, estuaries), the comparisons of the M_2 tidal component derived from a harmonic analysis of the surface and middepth currents (approximately 10 m) resulted in a mean difference of 22 cm s^{-1}, with a standard error of about 4 cm s^{-1}. Matthews et al. (1988) found rms differences of 16 cm s^{-1} between OSCR observations and moored current meter observations at 5 m below the surface north of Beaumaris Bay, United Kingdom. OSCR-derived surface current data have also been compared to observations acquired along five tracks of acoustic Doppler current profilers (ADCP) from the USNS *Bartlett* during the Office of Naval Research (ONR) and Naval Research Laboratory (NRL) High Resolution Remote Sensing Experiment (HIRES) pilot program in September 1991 (Herr et al. 1991). Average differences in the magnitude and direction of the surface and subsurface currents (15 m) from four of the five tracks of ADCP data ranged between 8 and 19 cm s^{-1} and 4° and 14°, respectively (Shay et al. 1992). Although these differences are sizable, the HF radar-derived surface current measurement represents an integrated value in the upper 0.5 m of the water column, whereas the ADCP currents were observed at 15-m depth. While differences are anticipated in a highly sheared baroclinic regime, such as the north wall of the Gulf Stream (GS) intruding over the shelf and slope, more measurements are required to establish the relationship between surface and subsurface signals.

TABLE 1. RSMAS OSCR system capabilities and specifications for the high-frequency mode.

Number of measurements cells	700
Operation range (km from radar site)	44
Range cell resolution (km)	1
Measurement depth (m)	0.4
Measurement cycle (min)	20
Accuracy	
Radial current (cm s^{-1})	2
Vector current (cm s^{-1})	4
Vector direction (°)	5
Data storage (days)	120
Operating frequency (MHz)	25.4
Transmit elements (yagi)	4
Receive elements (phased array)	16
Transmitter peak power (kW)	1
Transmitter average power (W)	2
Power consumption (kW @ 240 V)	1
UHF communications link (MHz)	458

As part of the ONR and NRL HIRES Research Program (Herr et al. 1991) and the Minerals Management Service (MMS) sponsored North Carolina Physical Oceanography Program (MMS 1991), an OSCR was deployed from June to July 1993 off the Outer Banks of North Carolina. The focus of the program's experimental effort was on the inshore edge of the north wall of the GS where research vessels, aircraft, moorings, and drifters acquired oceanographic and atmospheric observations from 11 to 28 June 1993 (Fig. 1). The experimental site was located on the innershelf to the shelfbreak where water depths change from 30 to 2000 m over a distance of about 80 km. The MMS current meter moorings (B_1, B_2) were deployed for a period of two years to characterize the circulation between the coast and the north wall of the GS, and to quantify cross-shelf exchanges of heat and momentum due to mesoscale features such as warm-core rings, meanders, filaments, and rips (Marmorino and Trump 1994).

The objective here is to assess the quality of the surface current measurements by directly comparing these data to time series of subsurface current meter measurements at the directional discus moorings; hereafter referred to as discus west (D_W) and discus east (D_E), which were sponsored by the ONR HIRES program. Given the cited measurement accuracy of the OSCR surface currents of 4 cm s^{-1}, this study quantifies the accuracy of the surface currents in several frequency bands over the nearly continuous 27-day time series, rather than just the tidal bands. The observed two-dimensional surface and subsurface velocity time series are decomposed into tidal, mean, near-inertial, and high-frequency bands to understand the vertical correlation (and decorrelation) scales in a highly sheared

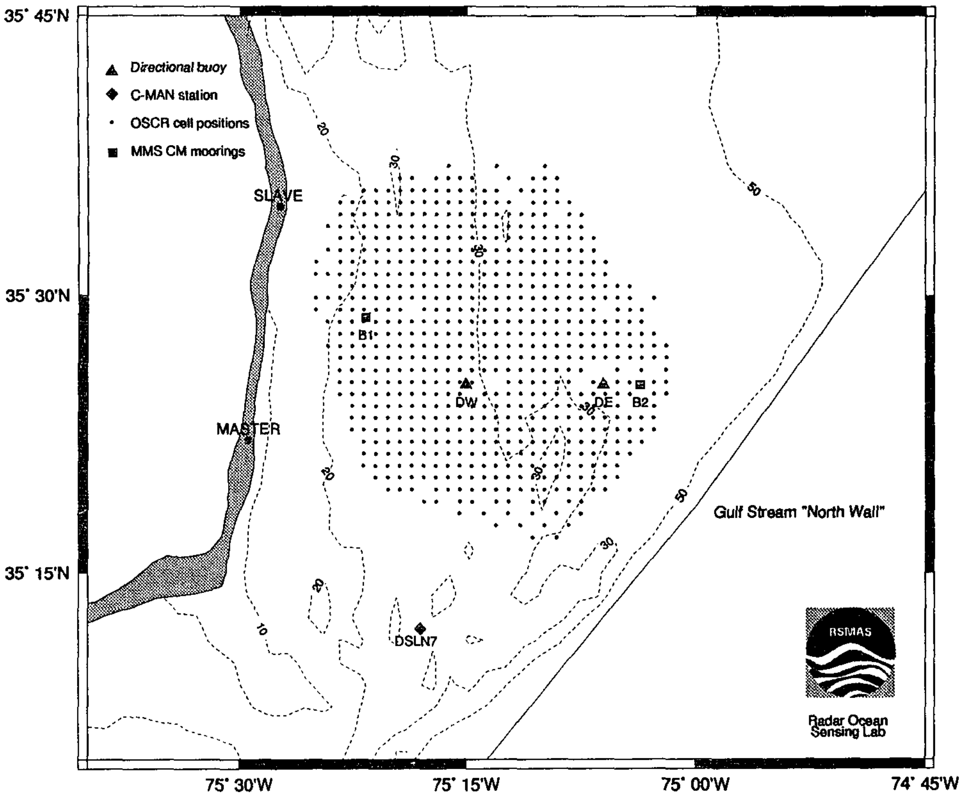

FIG. 1. Experimental domain of HIRES-2 off Cape Hatteras including the OSCR footprint (dots) encompassing the directional discus buoys (D_W and D_E) and MMS moorings (B_1, B_2) relative to the bottom topography (dashed) contoured in meters. The master and slave sites were located in Avon and Waves, North Carolina, respectively.

baroclinic zone. Statistical moments including variance between the surface and subsurface current signals and regression analyses are given to quantify the quality of observed surface current data from the HF radar technique.

2. Experimental design

a. Ocean surface current radar

The OSCR radar system was deployed for a jointly sponsored ONR/MMS study along Cape Hatteras from 11 June to 8 July 1993. The system consisted of two HF radar transmit–receive stations operating at 25.4 MHz, thereby sensing the scattered field from long surface gravity wavelengths of about 5.9 m (Table 1). The HF radar system mapped the coastal ocean currents over a 30 km × 44 km domain at 20-min intervals with a horizontal resolution of 1.2 km. The individual radars were located at two oceanfront sites in Avon (master) and Waves (slave), North Carolina, which equates to a baseline distance of 24 km. Each site consisted of a 4-element transmit and 16-element receiving array oriented at an angle of 30° to the beachfront (southeast–northwest at Avon and northeast–southwest at Waves) over a distance of 85 m.

During the first 5 min of the sampling interval, the master site transmits, receives, and coherently processes backscattered energy and interpolates the complex phase information from each of the 700 grid points. This entire process is repeated 896 times and takes less than five minutes, and the corresponding phase information for each cell are then Fourier transformed to form Doppler spectra. The frequency of the receding and advancing peaks in the Doppler spectra are used in computing the radial current value at each cell over the subsequent five minutes. One of the identified Bragg peak amplitudes (usually two Bragg peaks are present) must exceed the background noise level by 9 dB prior to calculating a current vector, otherwise no current vector is estimated from the Doppler spectra. During this period, the slave site transmits, receives, and processes its signals followed by five minutes of data reduction. Over the remaining five minutes of the sample cycle, slave data are sent to the master site via UHF radio link to combine radial currents into two-dimensional current vectors (speed and direction), store the time series, and display the surface current map. The manufacturer's cited accuracy of the radial and the vector speeds are 2 and 4 cm s^{-1}, respectively, and the directional resolution is 5°. These error estimates are a function of the spectral resolution, angle of intersection between the master and slave radial beams (Lipa and Barrick 1983), and the positioning accuracy of the antennas or boresight. Other effects such as atmospheric noise and sea echo may induce additional uncertainty in the velocity field or limit range performance (Barrick 1980).

Over the 27-day experiment, only 58 samples of the possible 1905 were not acquired. A large fraction of these missing samples occurred during the period of 2340 UTC 3 July–1300 UTC 4 July, when the receiving element array at the slave site was vandalized (Shay et al. 1993). The data return approached 97% averaged over the OSCR domain as shown in Fig. 2. The highest return (approaching 100%) occurred in the inshore region, decreasing seaward to a minimum of about 70% at the 44-km range—the theoretical limit of OSCR's range for the current configuration, which is based upon the pulse rate of the radar. At the extreme ranges (>40 km), normally only one Bragg peak in the spectra was available to calculate a radial vector.

b. *Surface current observations*

There were several days during the experimental period when interesting surface features appeared in the observations. Four cases are shown in Fig. 3 to illustrate the marked spatial variability in the surface circulation such as mesoscale eddies, convergence zones, and intrusions of the north wall of the GS over the shelf. On 15 June (Julian day 166), the research vessels were located in regions of considerable horizontal surface current variability in the OSCR domain (G. Marmorino 1993, personal communication). In the western part of the domain, cooler coastal currents of 20 cm s^{-1} were directed toward the south-southeast (Fig. 3a). Between B_1 and $\mathrm{D_W}$, the surface currents converged with a weak offshore flow of 15–20 cm s^{-1} at $\mathrm{D_E}$ and B_2. In addition to these features near B_1, high-frequency internal wave packets were observed at 35.5°N, 75°W during transects by the research vessels. Although this position was on the eastern perimeter of the OSCR domain, these packets may have propagated westward onto the shelf and into the domain.

On 23 June (JD 174), a cyclonically rotating eddylike feature was located toward the northeast of B_1 between the GS and the coastal current (Fig. 3b). Maximum surface currents were 50–75 cm s^{-1} in the southeast part of the OSCR domain and may have been due to the interactions between the coastal current and the GS. The GS moved farther offshore over the next 12–14 h and the eddylike feature dissipated; however, a convergence zone developed in the center of the OSCR domain between B_1 and $\mathrm{D_W}$ on the subsequent day (not shown).

The GS was located offshore on 28 June (JD 179) as relatively weak currents dominated the OSCR domain (Fig. 3c). Again, there were complex features such as a convergence zone and an eddy near B_1 where the observed currents were weak due to possible tidal modulations. The GS was well offshore as indicated by the currents of 25 cm s^{-1} directed toward the northeast in the southeast quadrant of the domain. Over the last two days of the experiment, the GS penetrated further onto the shelf with maximum speeds of about 1 m s^{-1} as shown in Fig. 3d. A convergence zone was also located between B_1 and $\mathrm{D_W}$. Thus, the relative consistency of the evolving snapshots indicated considerable submesoscale surface current structure [scales less than the deformation radius of $O(10$ km) for phase speed of $c_1 = 0.8$ m s^{-1}] excited by a cooler coastal current and intrusions of the north wall of the GS over the shelf break.

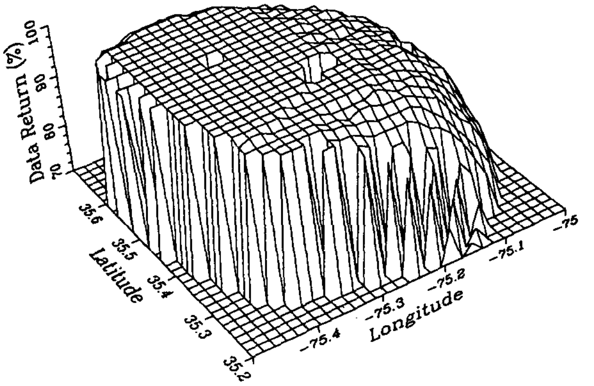

FIG. 2. Three-dimensional view of the percent of data return acquired by OSCR during the HIRES-2 experiment. The high data return drops off from 100% to a minimum of about 70% at about 44 km offshore.

c. *Buoy measurements*

The National Data Buoy Office directional discus surface buoys were equipped with a UCM 40 Mk II three-axis ultrasonic current meter that also included a conductivity–temperature–depth sensor manufactured by NE Sensortec A/S of Norway. Using built-in compass and tilt sensors, the instrument measured the horizontal and vertical currents over a 10-cm path with an accuracy of about 3% for an integration time as short as 1 s. The current measurements from the UCM-40 have a resolution of 0.1 cm s^{-1} (Table 2). During the HIRES-2 experiment, these instruments were deployed on $\mathrm{D_E}$ (35°25′N, 75°06′W) and $\mathrm{D_W}$ (35°25′N, 75°15′W) moorings at depths of 9.5 and 13.8 m, respectively. The instruments were configured to acquire data at a rate of 20 Hz for a 1-min duration over a 10-min sampling interval and recorded an averaged value for each sample interval.

d. *Observed time series*

The time series of observed winds, surface and subsurface currents and temperatures, the bulk vertical

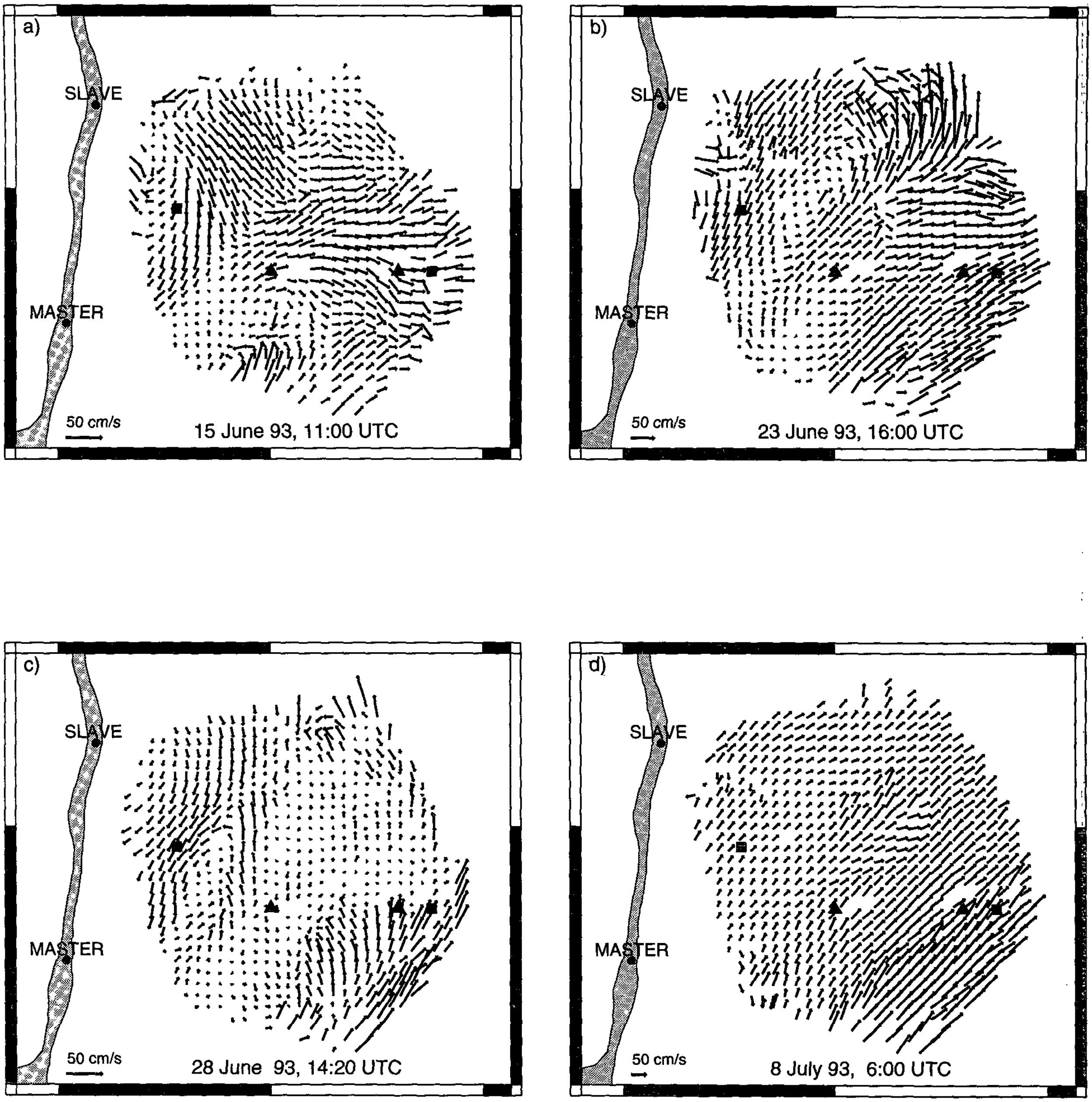

FIG. 3. Surface current maps from the HIRES-2 experiment at (a) 1100 UTC 15 June, (b) 1600 UTC 23 June, (c) 1420 UTC 28 June, and (d) 0600 UTC 8 July 1993. The boxes and circles depict locations of the directional discus mooring (D_W, D_E) and the MMS moorings B_1 and B_2 in the OSCR domain. Note that the velocity scale is 50 cm s^{-1} in each panel.

current vector differences (i.e., shears), and the complex correlation coefficients (defined below) at D_W and D_E are shown in Figs. 4 and 5, respectively. Given the relatively calm atmospheric conditions during the experiment, the wind speeds typically ranged from 3 to 5 m s^{-1}, and there were a few periods of time when the wind changed direction (Fig. 4a). To facilitate direct comparison to the OSCR surface currents at the D_W and D_E grid points, the subsurface current measurements were smoothed using a three-point Hanning window and subsampled at 20-min intervals. As shown in Figs. 4b,c, there was marked agreement between the surface and subsurface current components (u positive east, v positive north) at D_W that had magnitudes of about 50 cm s^{-1}. There were intervals of time when the current components oscillated over periods of a few hours superposed on longer timescale variations. Since these motions may have propagated along isopycnal (isothermal) surfaces, the surface and subsurface current signals were out of phase. As shown in Fig. 4d,

TABLE 2. Summary of the range, resolution, and accuracy of the three-axis ultrasonic current meter and a conductivity, temperature, and depth sensor instrumented on the D_W and D_E buoys in the HIRES-2 experiment.

Variable	Range	Resolution	Accuracy
Current velocity	±3 m s^{-1}	1 mm s^{-1}	3% (±5 mm s^{-1})
Sound velocity	1380–1580 m s^{-1}	2 m s^{-1}	±5 m s^{-1}
Temperature	−5° to +45°C	0.01°C	0.1°C
Pressure	0–50 b	0.04% FS	0.5% FS
Conductivity	2–77 mmho cm^{-1}	0.01 mmho cm^{-1}	0.06 mmho cm^{-1}
Compass	0°–360°	0.1°	±2°
Tilt sensors	±30°	1°	5%

the sea surface temperature (SST) and subsurface temperature time series between JD 164 and 168 indicated a temperature difference of 3°–5°C, which indicates that the mixed layer was less than 13.8 m over this time period. The cooler subsurface temperatures were due in part to the southward flowing coastal current dominating the nearshore flow regime. Notice that the oscillatory SSTs following this cold event had amplitudes of about 1°C consistent with the velocity fluctuations. In a bulk sense, vertical current shears (Fig. 4e) estimated from the surface and subsurface velocities were $O(10^{-2}\ s^{-1})$, which were found in velocity profiles acquired from the deployment of airborne expendable current profilers during the Surface Wave Dynamics Experiment in the GS (Shay et al. 1994).

One statistical measure of the relationship between the surface (u_o, v_o) and subsurface (u_b, v_b) current vectors is the complex correlation coefficient given by

$$\gamma = \frac{\langle u_o u_b + v_o v_b \rangle + \iota \langle u_o v_b + v_o u_b \rangle}{\langle u_o^2 + v_o^2 \rangle^{1/2} \langle u_b^2 + v_b^2 \rangle^{1/2}}, \qquad (1)$$

and the phase coefficient

$$\phi = \tan^{-1} \frac{\langle u_o v_b + v_o u_b \rangle}{\langle u_o u_b + v_o v_b \rangle}, \qquad (2)$$

where angle brackets represent a spatial or time average (Kundu 1976). Geometrically, this phase angle represents the average counterclockwise angle of the subsurface current vector with respect to the surface current vector. Daily averaged (72 points) complex correlation coefficients indicated several days of high correlation ($\gamma > 0.8$), and days when the higher-frequency oscillations significantly decreased the vertical correlation coefficient to less than 0.3 at both D_W and D_E (Figs. 4f and 5f).

The wind field at D_E indicated surface winds of 4–5 m s^{-1} (Fig. 5a), reflecting the weak variability in the atmospheric conditions during the experiment. Surface and subsurface currents at D_E were similar to those variations observed at D_W, but with more energy because of the closer proximity to the north wall of the GS (Figs. 5b,c) where the current components ranged from −25 to 75 cm s^{-1}. Periods of high correlation (>0.8) occurred when the higher-frequency motions were not present in the current variations. From JD 164 to 171, temperature differences (between the surface and subsurface levels) ranged between 1° and 4°C as shown in Fig. 5d. The diurnal variation in the SSTs occurred during these light wind conditions, as cooler, lighter shelf water overlaid the warmer GS water. The largest temperature change of about 4°C coincided with an offshore movement of the GS and the intrusion of the coastal current. As at D_W, there was a temperature oscillation of about 1°C during this time period when higher-frequency current oscillations were observed. As shown in Fig. 5f, large vertical phase differences between surface and subsurface layers suggested either a vertical decorrelation due to the shorter timescale oscillations or the passage of a front (i.e., experimental days 6 and 7).

Using the 1905 samples of the surface and subsurface velocities, the current components (u, v) were regressed based on linear least squares (Fig. 6). Mean biases and slopes between the components ranged from 2 to 4 cm s^{-1} and 0.77 to 0.93, respectively. The low scatter in the regression indicated fairly stable statistics. These slopes imply that the subsurface currents at 13.8 and 9.5 m were typically 10%–20% less than the OSCR-derived surface currents. However, there were periods when the subsurface currents exceeded the surface values, presumably due to the GS intrusions occurring at depth prior to a surface signature (i.e., JD 167–171). This intermittency in the current maxima is reflected in the histograms of the velocity differences for each component where the data follow a theoretical Gaussian distribution. That is, about 95% of the differences lie within the $\pm 1.96s$, where s is the standard deviation. The salient feature in the histograms is that over 50% of the current differences were within ±12 cm s^{-1} with the peak skewed toward positive values of 3–3.8 cm s^{-1} at D_W and 3.6–4.4 cm s^{-1} at D_E. As shown in Table 3, rms differences at D_W were 12.3 and 11.2 cm s^{-1} for the velocity components ($u_o - u_b$, $v_o - v_b$), respectively. Similarly, the velocity components at D_E ranged from 12.8 to 15.8 cm s^{-1} rms because of the proximity of the GS. In both cases, these rms differences were less than those found by Matthews et al. (1988) in Beaumaris Bay, United Kingdom.

3. Velocity decomposition

To examine the frequency content of the surface current signals at D_W and D_E, the rotary kinetic energy spectra (per unit of mass) were computed by decomposing the complex rotating vectors into the cyclonic and anticyclonically rotating components from the surface current time series in Figs. 4 and 5 (Gonella 1972). As shown in Fig. 7, the energy levels at the low frequencies were larger at D_E than at D_W because of

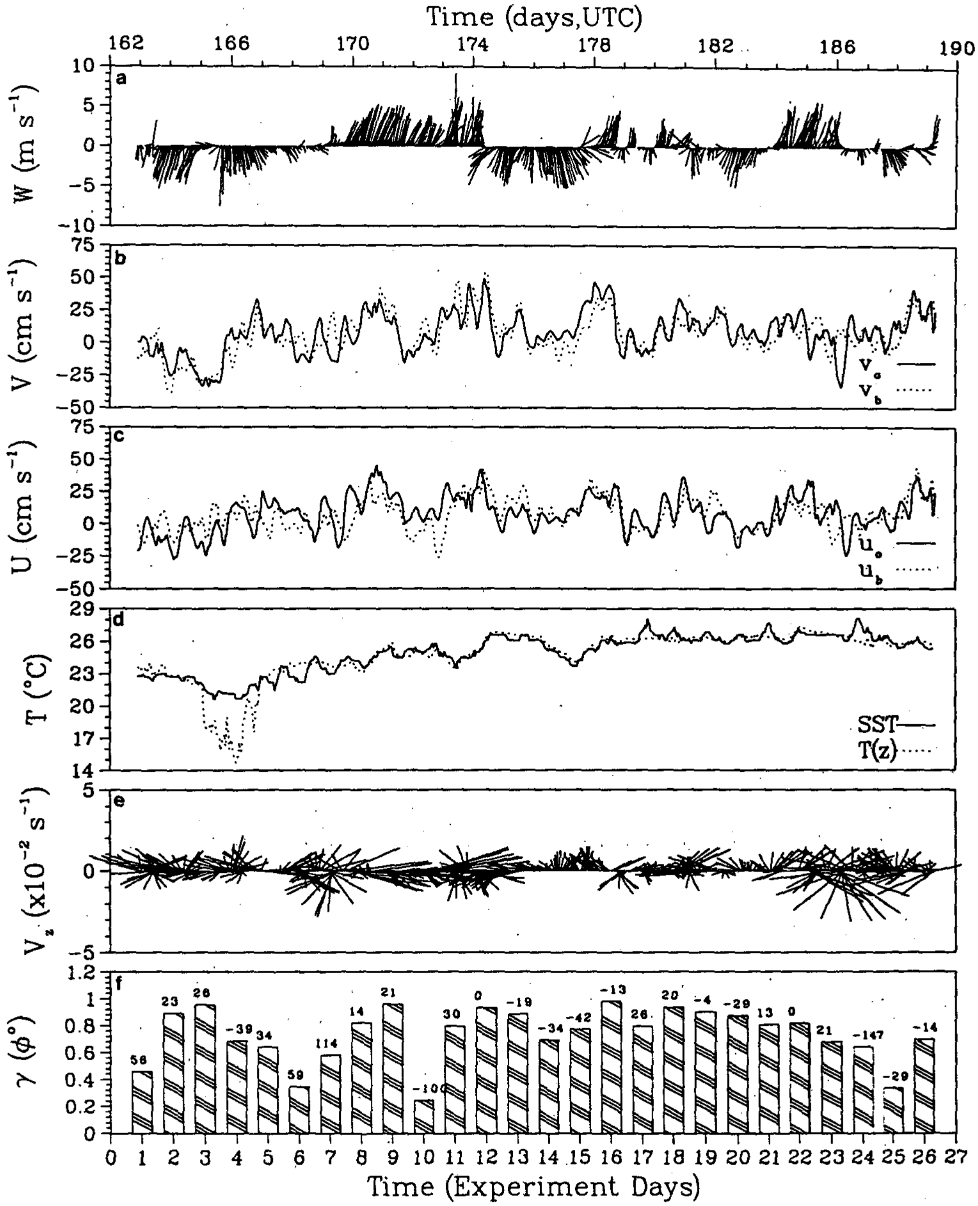

FIG. 4. Observed time series at D_W from 11 June to 8 July 1993 during HIRES-2 for the (a) wind vector, surface, and subsurface (b) north–south current components, (c) east–west current components, (d) sea surface and subsurface temperatures, (e) bulk vertical current vector differences over a 13.8-m layer, and (f) daily averaged (72 points) complex correlation coefficients and complex phases listed above each bar. Note that the wind vector represents the direction toward, as in an oceanographic sense.

its closer proximity to the North Wall of the GS. At both sites, the semidiurnal frequency tidal constituent (M_2) was the dominant peak in the spectra. For a sample interval of 20 min, this 12-h oscillation was defined by 36 points. Similarly, the diurnal tidal (K_1) and the inertial components (f) in the spectra, while not being dominant, indicated significant energy at the 24- and 20.7-h periods defined by 72 and 62 points, respectively. The lower energy levels for the anticyclonically rotating inertial period motions compared to the semidiurnal tides may be a manifestation of their intermittency associated with the GS intrusions onto the shelf. The peak in the band from 0.2 to 0.3 cph represents a 3–5-h oscillation as defined by 9–15 points. Similarly, this high-frequency peak does not dominate the cyclonically and anticyclonically rotating components; however, this oscillation is real since it is well below the Nyquist frequency of 1.5 cph and is also found in the subsurface current spectra (not shown). Beyond a frequency of about 1 cph, the spectra were

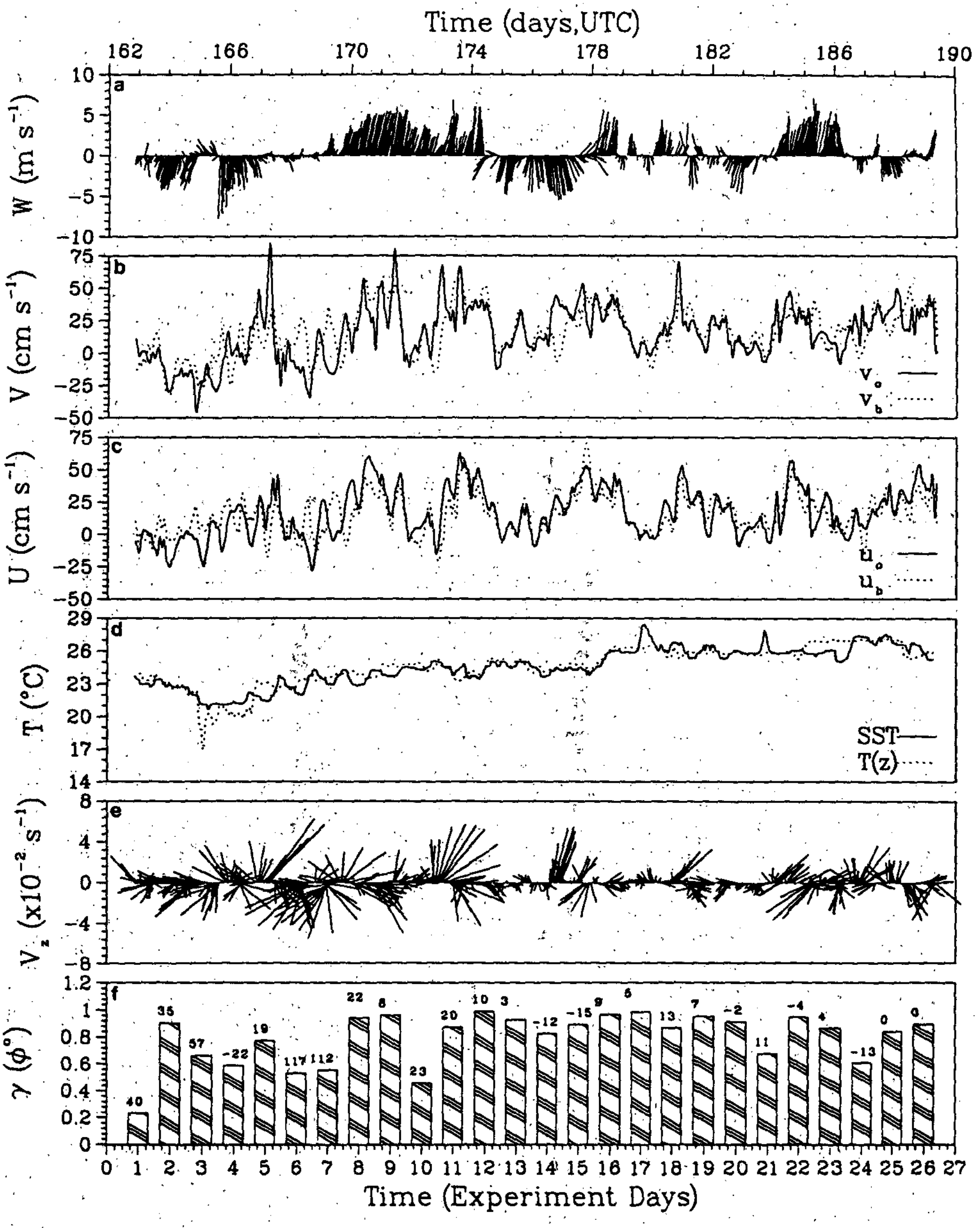

FIG. 5. Same as Fig. 4 except the observed time series at D_E and the bulk current vector differences [panel (e)] are estimated over a 9.5-m layer.

flat indicating less reliability in the measurements. Thus, spectral analysis indicates the presence of physical processes embedded in the HF-radar-derived surface current measurements that are resolved with a 20-min sampling interval.

The 27-day time series of surface and subsurface currents were decomposed into various components using digital filtering and harmonic analysis:

$$\mathbf{V}_{\mathrm{obs}} = \mathbf{V}_m + \mathbf{V}_t + \mathbf{V}_{\mathrm{in}} + \mathbf{V}_{\mathrm{hf}} + \mathbf{V}_r, \qquad (3)$$

where the subscripts obs, m, t, in, hf, and r represent the observed, mean, tidal, inertial, high frequency, and residual surface velocities, respectively. One component of the residual velocity is the Ekman wind-driven component. As noted in Figs. 4 and 5, the prevailing winds were relatively weak during the experiment, and the corresponding wave heights were also small having a mean of about 0.96 m and a standard deviation of 0.4 m. Thus, the wind- and wave-induced flows are beyond the scope of the present study.

The mean flow associated with the north wall of the GS and the coastal current structure accounted for 50%–70% of the variability as shown in Table 4. As expected, the variances were almost 50% larger at D_E

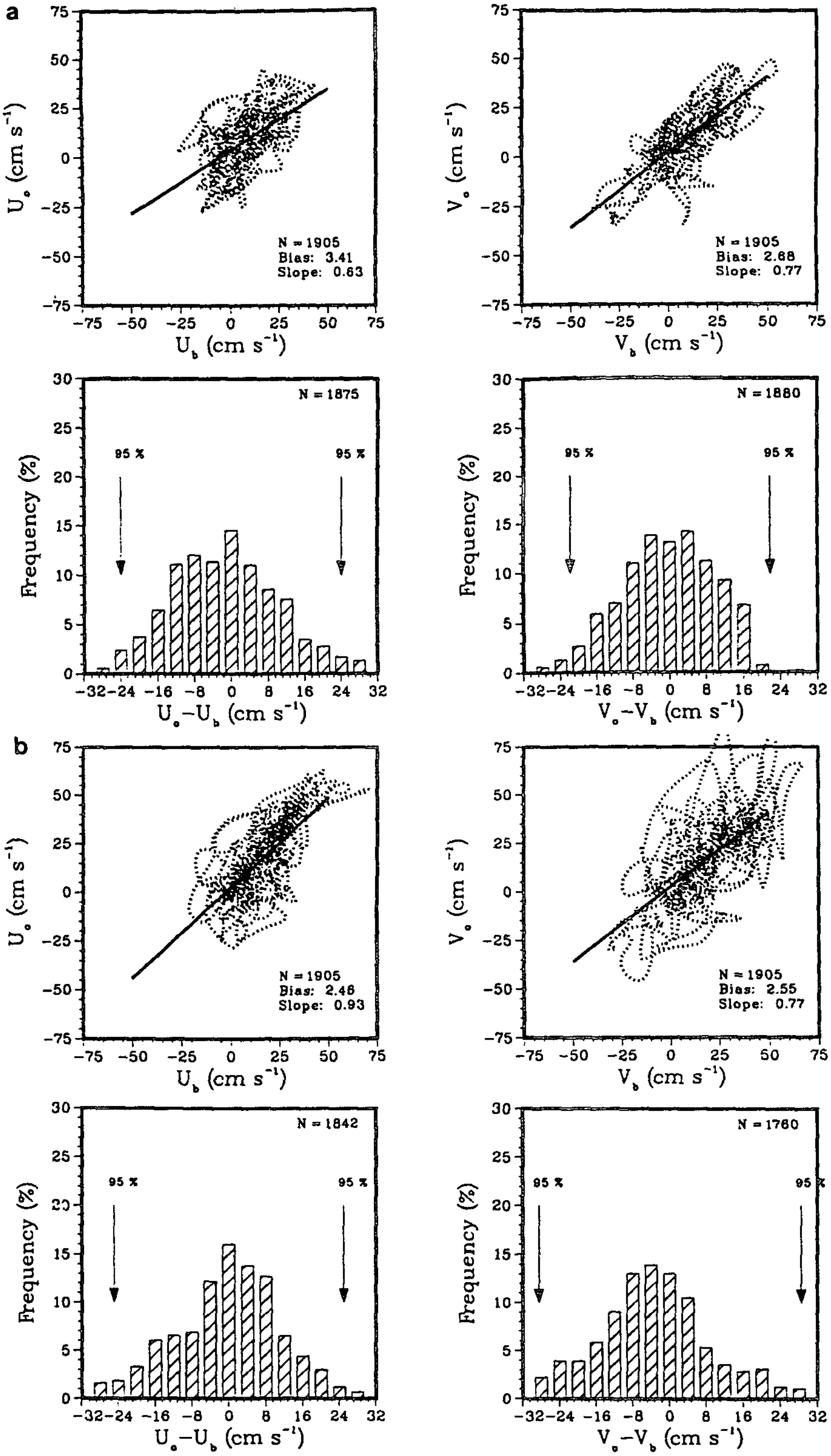

FIG. 6. Regression analyses of surface (ordinate) and subsurface (abscissa) currents (upper panels) and histograms for the current differences ($u_o - u_b$, $v_o - v_b$) (lower panels) (a) at D_W and (b) D_E in centimeters per second. The regression curves (solid) represent the best fit to the data with the bias and slopes given on the graphs. The histograms include differences of less than ±32 cm^{-1}, consistent with a vertical shear of 3×10^{-2} s^{-1} and the 95% confidence limits are depicted by arrows.

TABLE 3. Averaged difference between the surface and the subsurface currents for speed (V_{o-b}), direction (θ_{o-b}), east–west (u_{o-b}) component, north–south (v_{o-b}) component, complex correlation coefficient (γ), phase (ϕ), and the rms differences in the east–west ($u_{o-b_{rms}}$) and north–south ($v_{o-b_{rms}}$) velocity components based on 27-day time series as a function of frequency bands for the observed ($\mathbf{V}_{obs}$), tidal ($\mathbf{V}_t$), detided ($\mathbf{V}_d$), mean ($\mathbf{V}_m$), near-inertial ($\mathbf{V}_{in}$), and high frequency ($\mathbf{V}_{hf}$).

Series	V_{o-b} (cm s^{-1})	θ_{o-b} (°)	u_{o-b} (cm s^{-1})	v_{o-b} (cm s^{-1})	γ	ϕ (°)	$u_{o-b_{rms}}$ (cm s^{-1})	$v_{0-b_{rms}}$ (cm s^{-1})
D$_W$								
$\mathbf{V}_{obs}$	2.2	3.1	0.8	1.1	0.75	4.3	12.3	11.2
$\mathbf{V}_t$	−1.5	10.9	0.1	0.04	0.63	6.5	4.1	4.5
$\mathbf{V}_d$	2.6	3.9	0.73	1.03	0.76	4.0	11.5	10.1
$\mathbf{V}_m$	1.3	−1.2	0.75	1.02	0.88	4.3	7.7	5.7
$\mathbf{V}_{in}$	3.0	7.6	−0.02	0.01	0.33	179	6.2	6.5
$\mathbf{V}_{hf}$	−0.15	−2.6	−0.02	−0.02	0.03	−155	2.4	2.3
D$_E$								
$\mathbf{V}_{obs}$	2.6	−10.1	1.42	−1.28	0.84	4.0	12.8	15.8
$\mathbf{V}_t$	−1.8	6.0	0.07	0.03	0.76	2.5	3.6	5.9
$\mathbf{V}_d$	3.8	−11.0	1.34	−1.31	0.86	9.9	12.2	14.7
$\mathbf{V}_m$	2.9	−11.2	1.36	−1.32	0.95	8.3	7.3	8.4
$\mathbf{V}_{in}$	2.0	2.0	−0.01	−0.01	0.36	80.6	6.7	7.7
$\mathbf{V}_{hf}$	0.9	−0.5	−0.02	−0.01	0.06	−180	3.3	4.5

than at D$_W$ with larger variances in the north–south (v) than in the east–west (u) components. There was twice the variance in the surface u component at D$_E$ (243 cm^2 s^{-2}) than at depth (121 cm^2 s^{-2}), whereas the difference in the surface and subsurface variances for the u component at D$_W$ was about 19 cm^2 s^{-2}. Except for the u component at D$_E$, near-inertial variance exceeded the tidal variability in the surface layer at both sites but was less than the contribution of the tides in the subsurface layers particularly at 9.5 m. This may have been due to surface generation of near-inertial motions, whereas subsurface tidal maxima may have been the result of internal tides (Baines 1986). The contributions from the higher-frequency motions (3–5-h periods) accounted for a few percent of the total variance with larger values at D$_E$ of 7–15 cm^2 s^{-2}, and a factor 2–3 times larger at the surface than in the subsurface layers. Residual processes accounted for 8%–15% of the current variability.

a. Tidal analysis

The dominant semidiurnal (K_2, M_2, L_2, S_2) and diurnal (K_1, O_1, P_1, Q_1) tidal constituents were isolated from the surface and subsurface currents time series ($\mathbf{V}_t$) at D$_W$ and D$_E$ moorings by a least squares fit to

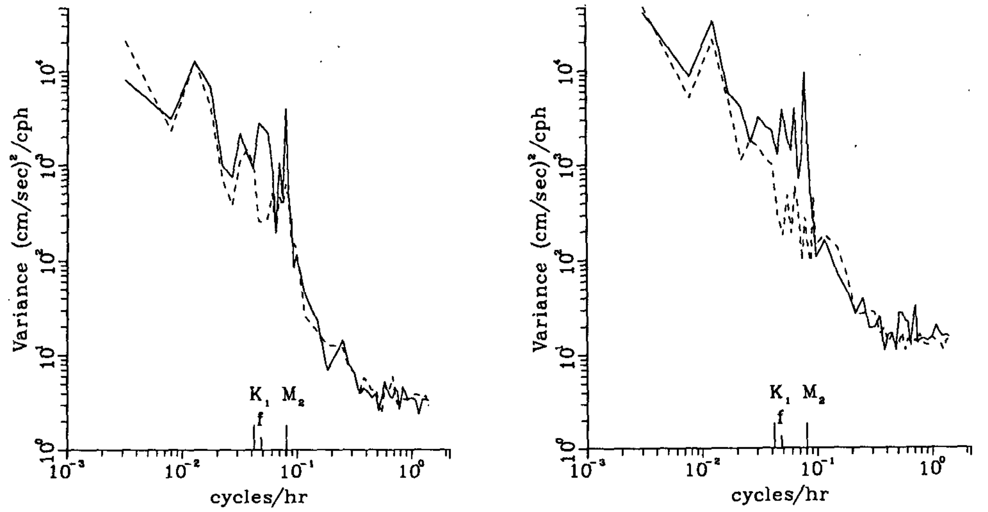

FIG. 7. Rotary kinetic energy spectra per unit of mass (cm^2 s^2 cph^{-1}) for the anticyclonically (solid) and cyclonically (dashed) rotating components calculated from the 27-day OSCR time series at D$_W$ (left panel) and D$_E$ (right panel). The frequencies (cph) of the tidal components M_2, K_1, and the inertial frequency f are depicted on the abscissa.

TABLE 4. Variances (cm^2 s^{-2}) of the OSCR (subscript *o*) and the D$_W$ and D$_E$ subsurface buoy measurements (subscript *b*) at 10 m during HIRES-2 experiment for the observed (V_{obs}), tidal (V_t), detided (V_d), mean (V_m), near-inertial (V_{in}), high frequency (V_{hf}), and residual (V_r) over the 27-day experimental period.

	V_{obs} (cm^2 s^{-2})	V_t (cm^2 s^{-2})	V_d (cm^2 s^{-2})	V_m (cm^2 s^{-2})	V_{in} (cm^2 s^{-2})	V_{hf} (cm^2 s^{-2})
D$_W$						
u_o	193	16	177	117	30	2
v_o	255	18	237	168	30	3
u_b	150	24	126	98	10	4
v_b	249	36	213	180	8	2
D$_E$						
u_o	360	37	323	243	31	7
v_o	440	32	408	284	44	15
u_b	221	54	169	121	19	5
v_b	345	62	282	235	17	5

each of the tidal constituents. As shown in Table 5, the dominant semidiurnal tidal constituents were the M_2 and to a lesser extent K_2 and S_2, whereas the more energetic diurnal tides were K_1 and P_1 constituents. The variance explained by a linear combination of the semidiurnal and diurnal tidal components ranged from 7% to 15% at D$_W$ with more tidal contributions to the subsurface records. In terms of variance, this equated to about 16–18 cm^2 s^{-2} at the surface and 24–36 cm^2 s^{-2} at depth. At the deeper site, explained surface current variances were 7%–10%, whereas values up to 24% were found at 9.5 m beneath the surface. Tidal variability at this depth was 53–62 cm^2 s^{-2}, or almost twice that of the surface of 31–37 cm^2 s^{-2}. The smaller surface tidal velocities may have been due to the interaction of the barotropic tide with the bottom topography, which excites baroclinic internal tides over the shelf break (Baines 1986). However, differences between the surface and subsurface velocity components ranged between 2 and 5 cm s^{-1} with the exception at D$_E$ where the difference was 7.7 cm s^{-1} for the K_1 constituent in the north–south direction. These estimated differences were less than those found in previous studies (i.e., Prandle 1987).

b. Detided flow

Based upon the amplitudes and phases of the tidal constituents in Table 5, the diurnal and semidiurnal tidal currents were removed to form a detided (i.e., $V_{obs} - V_t$) time series. At D$_E$, the surface and subsurface north–south velocity component v agreed well over

TABLE 5. Amplitudes (u, v) and phases (ϕ_u, ϕ_v) of diurnal and semidiurnal tidal constituents derived from a harmonic analysis of the OSCR surface currents (subscript *o*) and the D$_W$ and D$_E$ subsurface buoy measurements (subscript *b*) at 10 m during HIRES-2 experiment. The observed (σ_o^2) and predicted (σ_p^2) variance and the explained variance (%) by these constituents are also given.

Var.	K_1	O_1	P_1	Q_1	K_2	M_2	L_2	S_2	σ_o^2	σ_p^2	Expl. var. (%)
	(cm s^{-1})								(cm^2 s^{-2})		
D$_W$											
u_o	4.3	1.8	3.9	1.7	1.6	4.6	0.7	2.4	193	16.4	8.3
v_o	4.1	2.0	3.1	2.9	2.0	4.3	0.9	1.2	255	18.5	7.0
ϕ_u	0	−2	−2	0	1	3	−2	1			
ϕ_v	3	−2	0	0	2	−1	−2	1			
u_b	7.8	3.9	6.4	0.8	1.7	4.1	0.8	1.2	151	23.7	15.7
v_b	4.9	4.7	2.7	1.7	1.8	4.1	0.8	1.2	249	36.4	14.6
ϕ_u	−1	2	3	0	1	3	2	−2			
ϕ_v	−1	−3	−3	0	2	−1	3	−1			
D$_E$											
u_o	3.5	2.4	5.7	3.0	3.5	7.2	1.0	3.4	360	37.1	10.4
v_o	5.2	3.9	4.9	1.5	1.6	6.4	1.7	1.2	440	31.6	7.2
ϕ_u	0	2	−2	0	0	3	2	−3			
ϕ_v	0	3	−3	0	1	−2	−3	−2			
u_b	7.9	4.9	8.0	0.8	3.3	7.9	1.2	4.6	221	53.6	24.0
v_b	12.9	6.1	7.9	1.6	0.7	5.2	1.7	0.7	345	62.3	18.1
ϕ_u	−2	2	2	1	1	3	2	−2			
ϕ_v	−1	−3	3	−2	1	−2	3	3			

the time series (Fig. 8). Between JD 170 and 171, the subsurface v component was again about 5–10 cm s^{-1} larger than the surface current, followed by a similar difference on JD 173 when the surface v component was about 20 cm s^{-1} larger than the subsurface current. During the period from JD 172 to 174, the velocity components indicate the presence of high-frequency oscillations, and bulk vertical current shears of about 3×10^{-2}–4×10^{-2} s^{-1} that were directed toward the southeast. These velocity oscillations contributed to a reduction in the complex correlation coefficient from values of greater than 0.85 decreasing to less than 0.6 on experimental day 10 (JD 172) compared to a correlation coefficient of 0.5 found on the same day at D_W (not shown). However, it should be noted that the currents were weak at both stations on this particular day. Although over most of the 27-day time series the daily averaged correlation coefficients exceeded 0.6 at D_E, coefficients of 0.6 or less occurred on days 6, 7, 10, and 25 at D_W. The lower values were associated with large vertical current shears of 2×10^{-2}–3×10^{-2} s^{-1} oriented toward the south to southeast except on the first experimental day. When the north wall of the GS meandered across the shelf break, higher-frequency motions were advected and possibly trapped in the upper ocean by the stratification that tended to decorrelate surface and subsurface currents.

Regression analyses of the detided records at D_E indicated that the mean biases and slopes at D_E were reduced to 1.2–1.4 cm s^{-1} compared to 2.5 cm s^{-1} (Fig. 9). The slopes changed from 0.93 and 0.77 to 1.01 and 0.85, respectively. This suggests that when averaged

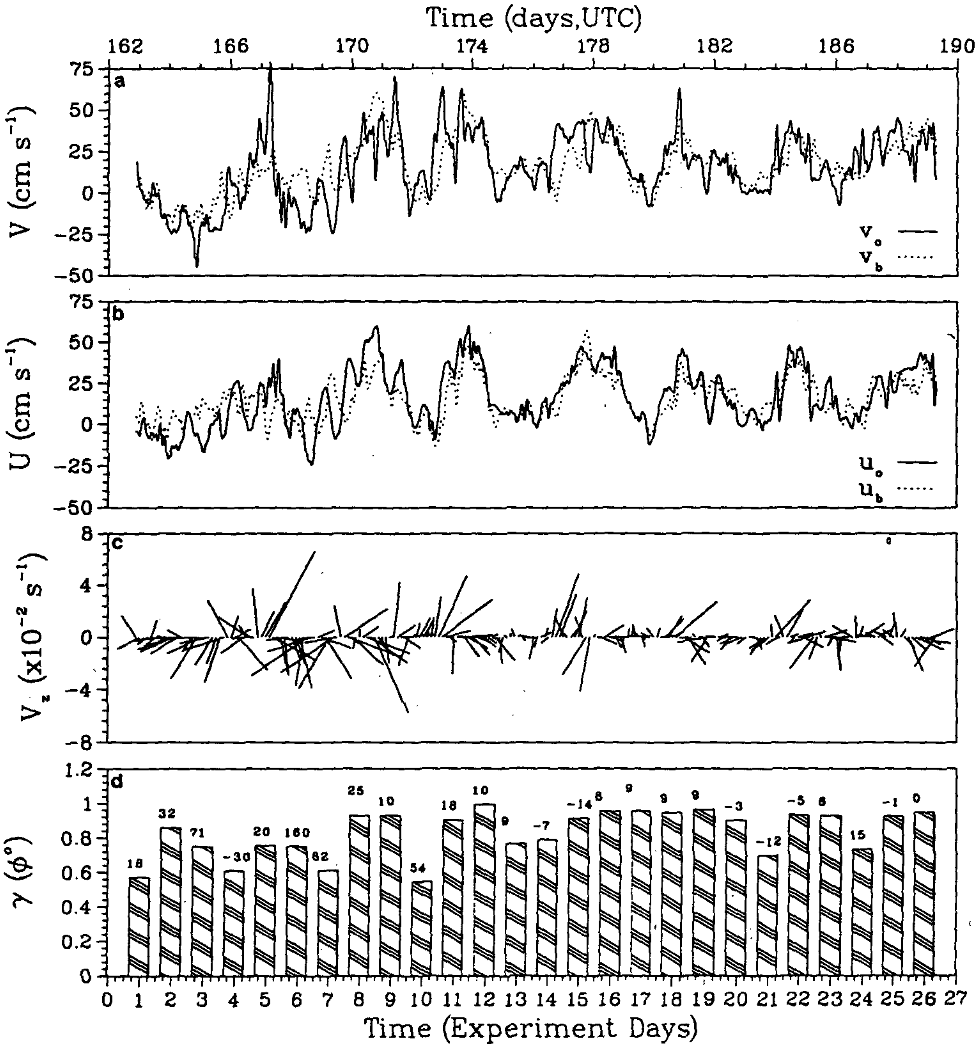

FIG. 8. Detided surface and subsurface current time series (V_d) at D_E from 11 June to 8 July 1993 for the (a) north–south current components, (b) east–west current components, (c) bulk vertical current vector differences over a 9.5-m layer, and (d) daily averaged (72 points) complex correlation coefficients and complex phases listed above each bar.

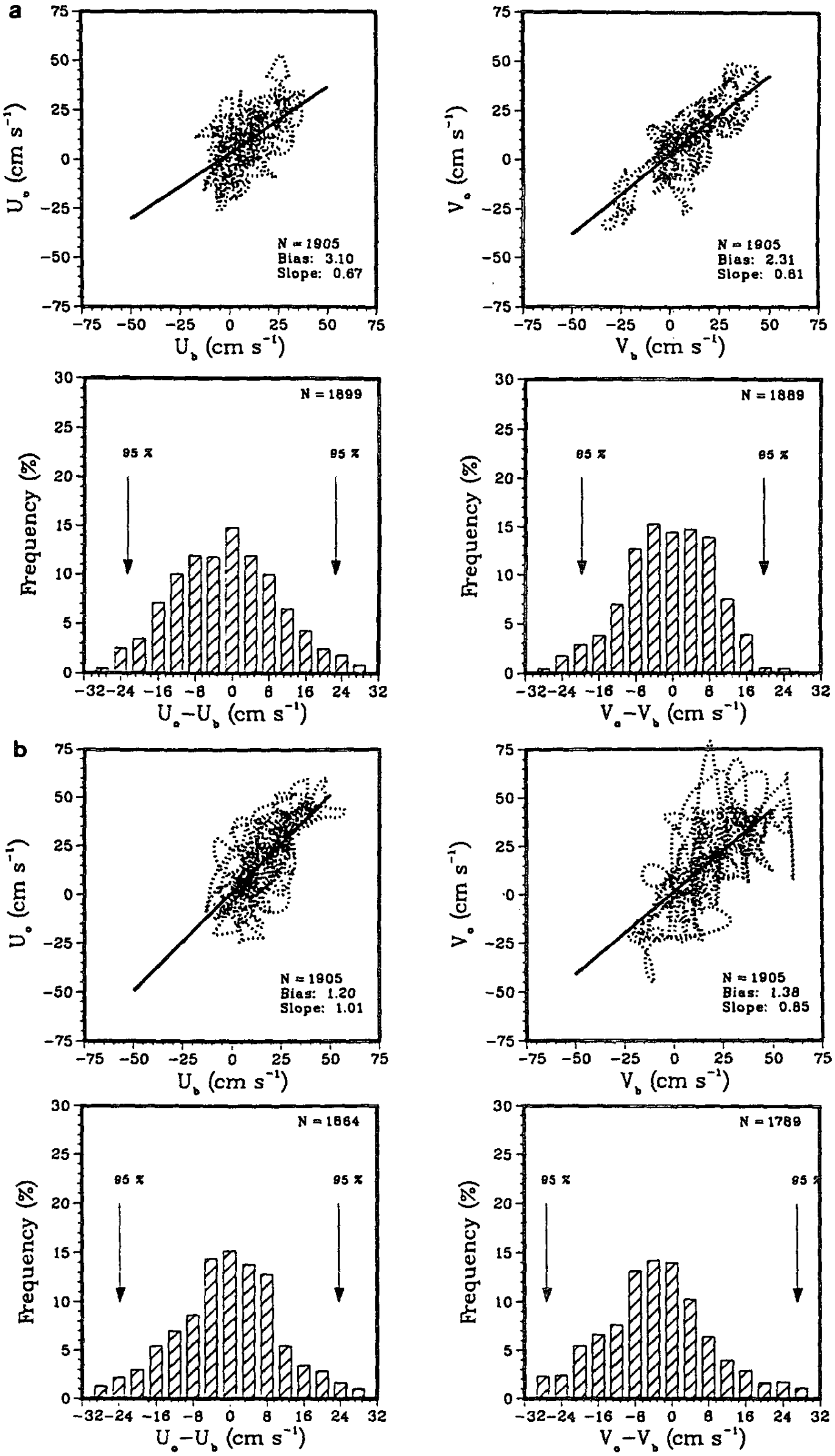

FIG. 9. Same as Fig. 6 except for detided surface and subsurface currents shown in Fig. 8.

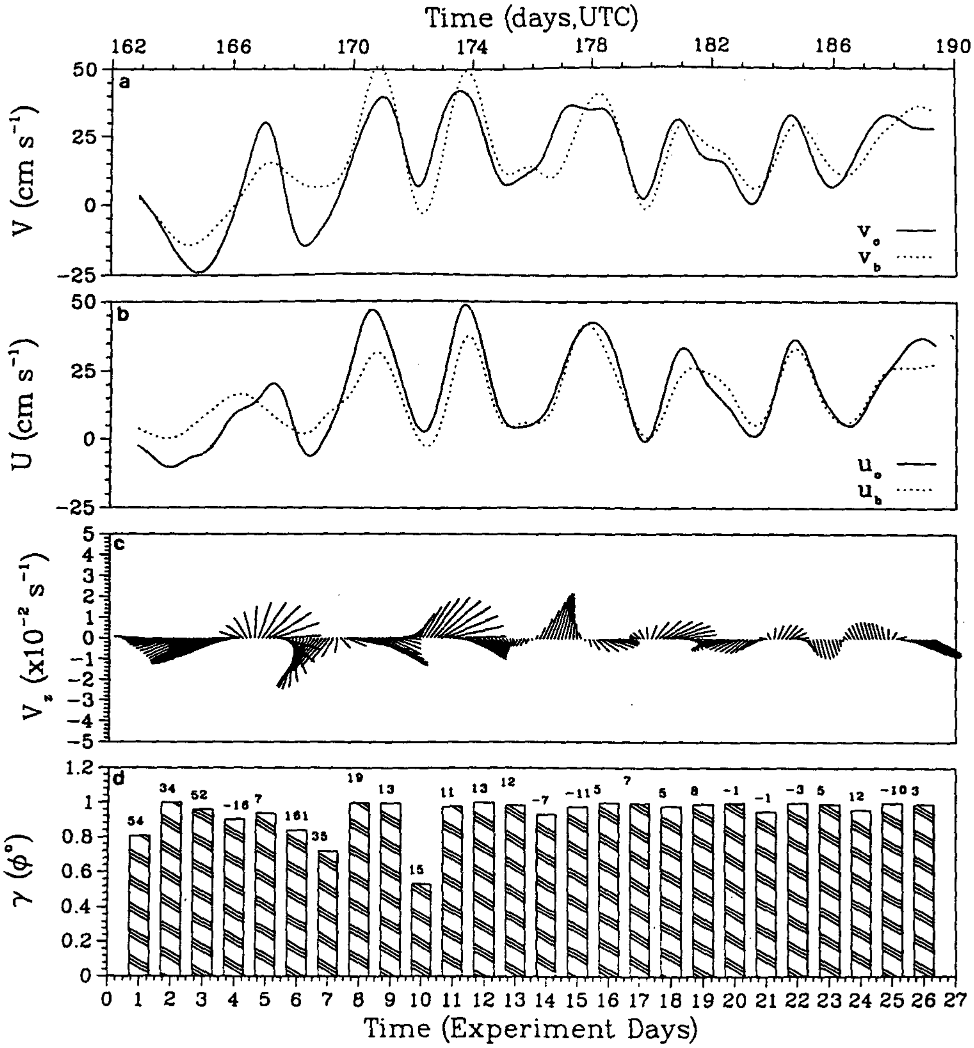

FIG. 10. Same as Fig. 8 except for detided, low-pass-filtered surface and subsurface current time series (V_m) at D$_E$.

over the time series, surface and subsurface east–west velocities were about equal, whereas north–south currents at depth were about 10%–15% less than at the surface. The histograms indicate that removing the tidal constituents from the observed currents tightened the distribution by about 3%–5% from those shown in Fig. 6. The rms differences between the surface and subsurface currents were reduced from 12.3 and 11.1 cm s^{-1} to 11.5 and 10.1 cm s^{-1} at D$_E$. A similar reduction in the rms differences of 0.8–1 cm s^{-1} was found at D$_W$ where the biases ranged from 3.4 to 3.1 cm s^{-1} and 2.7 to 2.3 cm s^{-1} in the east–west and north–south components, respectively. However, regression slopes increased by only 0.04 after removing the tidally driven flow.

c. Mean flow

To examine the longer-period current oscillations contained in the detided data, the surface and subsurface data were low-pass filtered at 48 h using a Lanczos-squared window to form a mean (V_m) time series. Since D$_E$ was located inshore of the climatological mean position of the north wall of the GS (Fig. 1), one of the striking features in the mean currents were the 3–5-day intrusions of the GS onto the shelf (Fig. 10). There were times when the subsurface v component exceeded the surface component (JD 174) by 10 cm s^{-1}. Four days later, the surface current increased by about 8–10 cm s^{-1} in the north–south direction. The differences between the surface and subsurface current components were more apparent in the east–west component because of the meandering nature of the GS intrusions, especially on JDs 166 and 181. Vertical current shears of $O(10^{-2}\ \mathrm{s}^{-1})$ indicated a complex, yet consistent current vector rotation as the GS intruded onto the shelf. The correlation coefficients were greater than 0.9 prior to day 10 (the time of low current velocities)

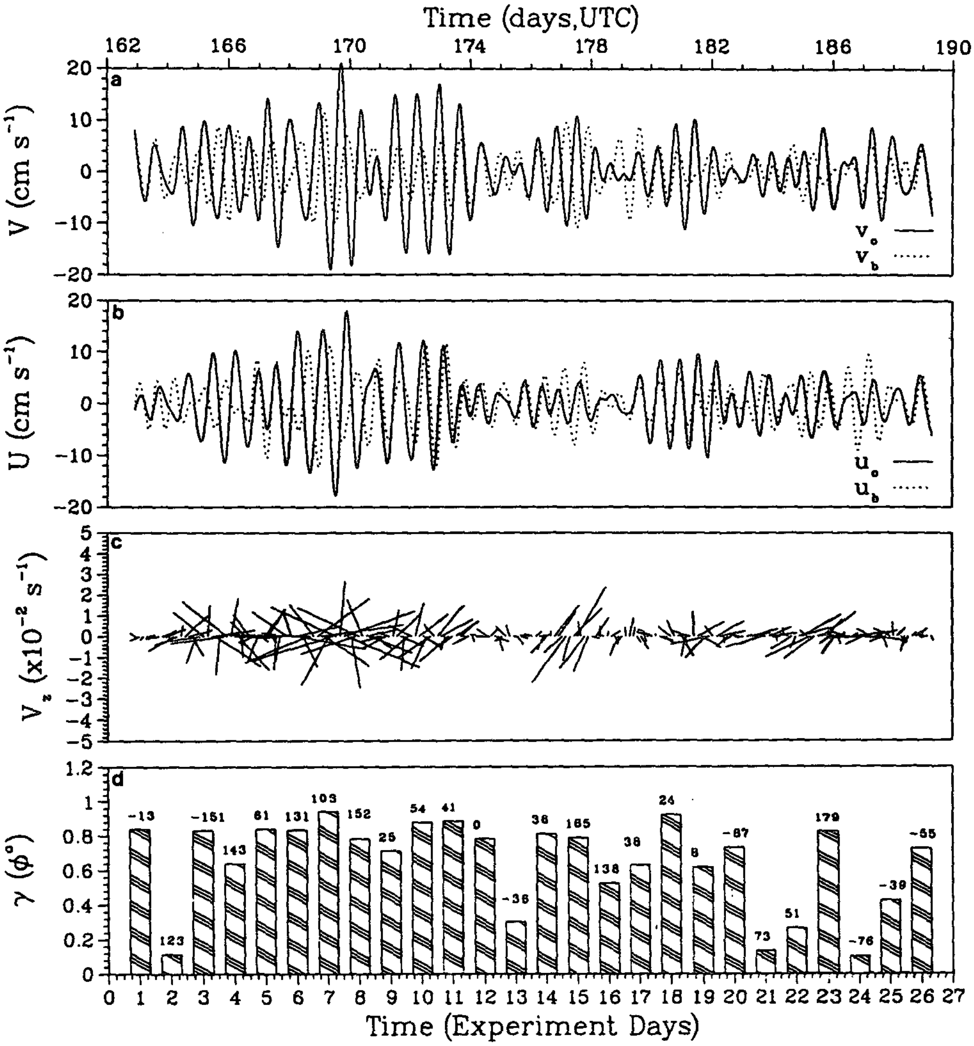

FIG. 11. Same as Fig. 8 except for detided, bandpass-filtered surface and subsurface current time series (V_{in}) at D_E.

when the correlation coefficient decreased to a level of 0.5. This coefficient remained at a level of greater than 0.9 over the remainder of the time series. Thus, the vertical correlation scale for the mean flow was larger than 9.5-m depth of the current meter at D_E. Similar trends were found at D_W, but with less energy as reflected in Table 4.

For the 1905 samples, biases for the mean currents were of 3.1 and 2.2 cm s^{-1} for the u components at D_E and D_W, respectively (not shown). However, for the v component, biases were 0.6 and 1.8 cm s^{-1}, which were markedly less than those in the east–west direction. This may be due to GS intrusions inducing more variability in the cross-shelf than the along-shelf directions. The slopes ranged from 1 to 1.3 at D_E, and 0.8 to 0.9 at D_W, which implies that the surface currents were more dominant than the subsurface currents at D_E, whereas the subsurface currents were slightly more energetic at D_W.

d. Near-inertial oscillations

The detided time series were bandpass filtered at 18 and 23 h using a Lanczos-squared window to form near-inertial current (V_{in}) time series evident in the anticyclonically rotating component in the rotary spectra [inertial period (IP) of 20.7 h] (Fig. 11). At D_E, the intermittent near-inertial current oscillations had maximum amplitudes of ±20 cm s^{-1} at the surface, with corresponding subsurface components of ±12–15 cm s^{-1}. There were obvious periods (i.e., JD 170 and 186) of vertical phase differences of 90°–180° between the surface and subsurface oscillations. These vertical phase differences suggest a vertical decoupling scale of

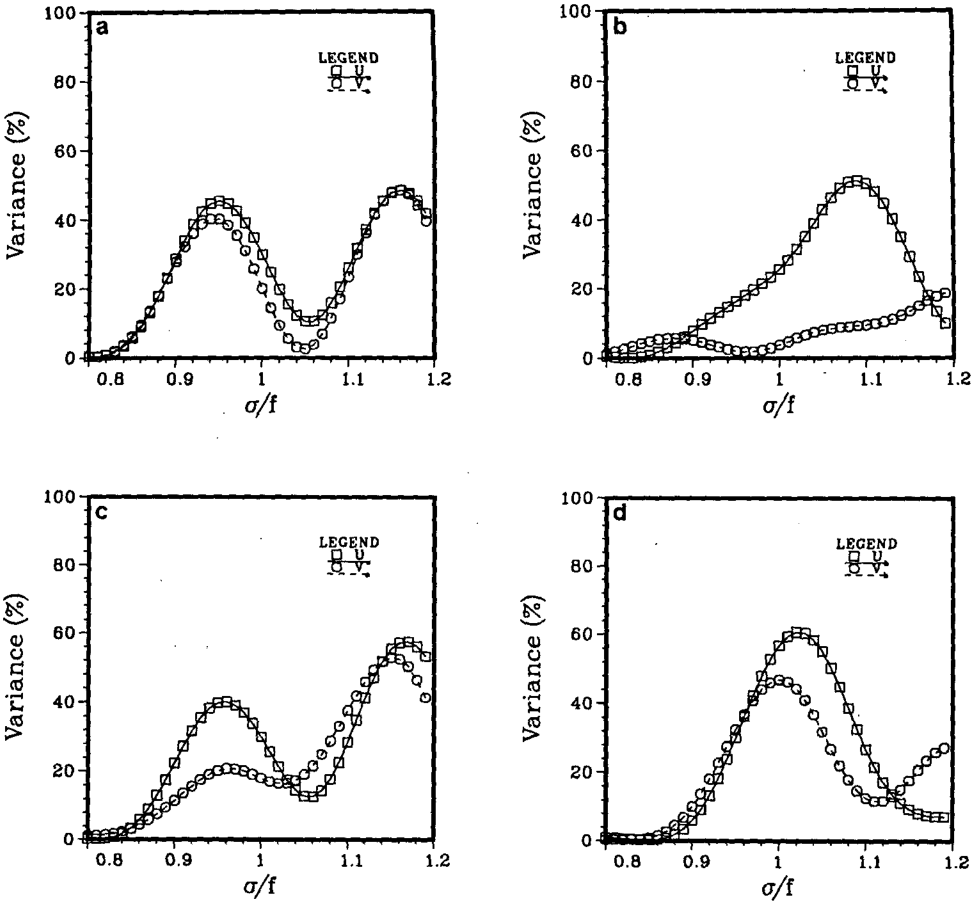

FIG. 12. Near-inertial frequency analysis for (a) D_W surface, (b) D_W subsurface, (c) D_E surface, and (d) D_E subsurface (u—squares) and (v—circles) components from 0000 UTC 14 June to 2340 UTC 20 June 1993. The ordinate represents explained variance (%) and the abscissa depicts frequency σ of the oscillations normalized by the local Coriolis parameter f.

less than 9.5 m either because of a shallow mixed layer, or a change in the vertical stratification between the water masses in water depths of 30 m. The correlation coefficients were less than 0.4 on experimental days 2, 3, 13, 21, and 24 due in part to the vertical phase differences of 123°, −36°, 73°, and −76°, respectively. Similar trends found at D_W on experimental days 3, 4, 9–11, 17, 21, and 26 were associated with fairly large phase differences between surface and subsurface signals. Between experimental days 16–18 (JD 178–180), near-inertial currents and the shears of 1×10^{-2}–$2 \times 10^{-2}\ \mathrm{s}^{-1}$ were in phase suggesting a mixed layer deeper than the current meter at the 9.5-m depth. While there were periods of high correlations, the complex correlation coefficients were less than those estimated from the low-pass-filtered records. Averaged over the 27-day record (see Table 3), the correlation coefficients at both D_E and D_W were 0.36 and 0.33 and phases were 81° and 179°, respectively.

To determine the frequency of the near-inertial motions from the current measurements, the bandpass-filtered time series were fit to a series of trial frequencies (typically 0.8–1.2f) over the 5–7 IPs. For a series of trial frequencies, a set of weights (u_1, u_2) were determined from the expression

$$u(t) = u_1 \cos(\sigma t) + u_2 \sin(\sigma t) + u_r, \qquad (4)$$

where σ is the trial frequency, and u_r is the residual current after the removal of the signal at that frequency (Shay and Elsberry 1987) with a similar expression for the v component. The product of the residual currents (viz $\langle u_r, v_r \rangle$) averaged over the appropriate time frame forms a covariance between the velocity components at zero lag. The carrier frequency is defined as the frequency that minimizes the covariance of the residual currents. The statistical uncertainty in the carrier frequencies is about 0.02f using this approach for a 20-min sample interval.

Over an approximate 7 IP cycle from 0000 UTC 14 June to 2340 UTC 20 June, the relative maxima in explained variance were shifted 5% below f to about 10% above f with dominant peaks at 0.97f and 1.1f

at D_W (Fig. 12). The carrier frequencies were $0.95\sigma/f$ and $1.14\sigma/f$ in the surface and subsurface signals, respectively. Explained variances in the u and v surface components were 45% and 41% at $0.95\sigma/f$, whereas values of 49% for both components occurred at $1.17\sigma/f$. In regimes of anticyclonically and cyclonically rotating mean flow vorticity, the frequency of the near-inertial motions is shifted below and above f, respectively (Kunze 1985). In the anticyclonically rotating vorticity regimes, near-inertial motions are trapped, whereas in cyclonically rotating vorticity zones these oscillations are focused into tight beams (convergence of wave rays), allowing the near-inertial waves to propagate from the area. Although the inner edge of the north wall of the GS supports a cyclonically rotating vorticity zone, a significant fraction of the near-inertial energy was shifted below f (0.9–0.97) with similar trends found in the surface near-inertial signals at D_E due in part to curvature effects. In fact, between JD 167 and 169 both anticyclonically and cyclonically rotating flow regimes were apparent in the mean flow fields in the vicinity of the B_1 and D_W moorings. The explained variances were a maxima at $1.17\sigma/f$ with values of 57% and 53% for u and v components, respectively. Subsurface near-inertial velocities were predominately shifted from 0.99 to $1.04f$ at D_E, and the minima in residual covariance were shifted to $1.02\sigma/f$. This blue shift is consistent with either a cyclonic shear zone of the mean flow or surface intensification, which seems unlikely given the quiescent winds that prevailed during the experiment (see Figs. 4, 5).

e. High-frequency motions

The detided time series were high-pass filtered at 8 h using a Lanczos-squared taper window to examine high-frequency (V_{hf}) surface and subsurface current time series containing oscillations with periods of about 4.5 h as suggested by the 0.2–0.3-cph oscillation in Fig. 7. As shown in Fig. 13, the amplitudes of these oscillations were ±10–15 cm s^{-1} at D_E, whereas values of up to 5–8 cm s^{-1} occurred at D_W (not shown). In some instances, subsurface oscillations exceeded the surface components in the east–west direction. Generally, the north–south components were larger at the surface than at depth. Notice that the vertical current shears were 10^{-3} s^{-1} or about a factor of 2 or 3 less than in the other frequency bands. The salient feature here was that the correlations were significantly less than in any of the other frequency bands, reaching a maxima of 0.5 at D_E and 0.35 at D_W for daily averaged values. Averaged over the 27 days, the correlation coefficients and phases were 0.1 or less and 100°–180° (Table 3). Since the bursts of high-frequency energy were correlated with the mean flow intrusions (Fig. 10), one possibility is that these motions propagate along the sloping isopycnals (isothermals) in a stratified flow over the shelf. Note that this 4.5-h oscillation (13–14 values) is within the internal wave band, which ranges from the buoyancy to the Coriolis frequencies (Baines 1986). For a 4.3–4.7-h oscillation, the frequency was about 3.8×10^{-4} s^{-1} compared to estimates of the buoyancy frequency 0.7×10^{-2}–1×10^{-2} s^{-1} based on the vertical temperature gradients (not shown). While the physics of the generating mechanisms and the dispersion of these higher-frequency motions (i.e., Ruddick and Joyce 1979; Olbers 1981; Brown and Owens 1981) are beyond the scope of this study, these oscillations (periods of 3–5 h) were not only detected by the HF radar but were measured by the subsurface current meters at the corresponding location sampling at 10-min intervals.

To examine the frequency content of one of the bursts in Fig. 13, the high-frequency surface and subsurface time series from 1800 UTC 15 June to 0600 UTC 17 June were fitted to a series of trial frequencies using (4) ranging from $0.5\sigma/N$ to $1.5\sigma/N$, which encompasses the 3–6-h span with a center point at 4.5 h. This center point has a frequency of 0.22 cph that is considerably less than the Nyquist frequency of 1.5 cph, which implies that these motions were not aliased. As shown in Fig. 14, the relative minima in the residual covariance occurred at $\sigma/N = 0.7$ in the surface current at D_W accounting for 30% of the variance in the v component. In the subsurface layer at D_W peaks for the velocity components were located at $0.8\sigma/N$ and $0.95\sigma/N$, yielding a minimum in the residual covariance at a carrier frequency of about $0.8\sigma/N$. At D_E, there was a spectrum of high-frequency current oscillations with peaks ranging from $0.6\sigma/N$ to about $1.3\sigma/N$ in the surface and subsurface layers. However, the relative minima in residual covariance of the surface and subsurface current signals were at $1.1\sigma/N$ and $0.7\sigma/N$. One possible reason for the larger differences between the surface and subsurface values at D_E was due to the closer proximity of the mooring to the GS. Surface and subsurface explained variances in the v component were correlated at $0.6\sigma/N$, whereas at other frequencies within this band, there were significant differences in the current variability. The point is that the superposition of two or more waves with different frequencies and wavenumbers may combine to form another wave with slightly different characteristics, yet in the vertical the signals will remain vertically decoupled because of the phase differences. This physical situation is accentuated in strongly sheared baroclinic regimes intruding over the continental shelf break (Marmorino and Trump 1994) or over sills separating two water masses during tidal cycles (Wesson and Gregg 1994).

4. Summary

The OSCR system was used in a major U.S. field program to successfully measure the surface currents and their gradients in a complex regime dominated by a meandering western boundary current. The OSCR

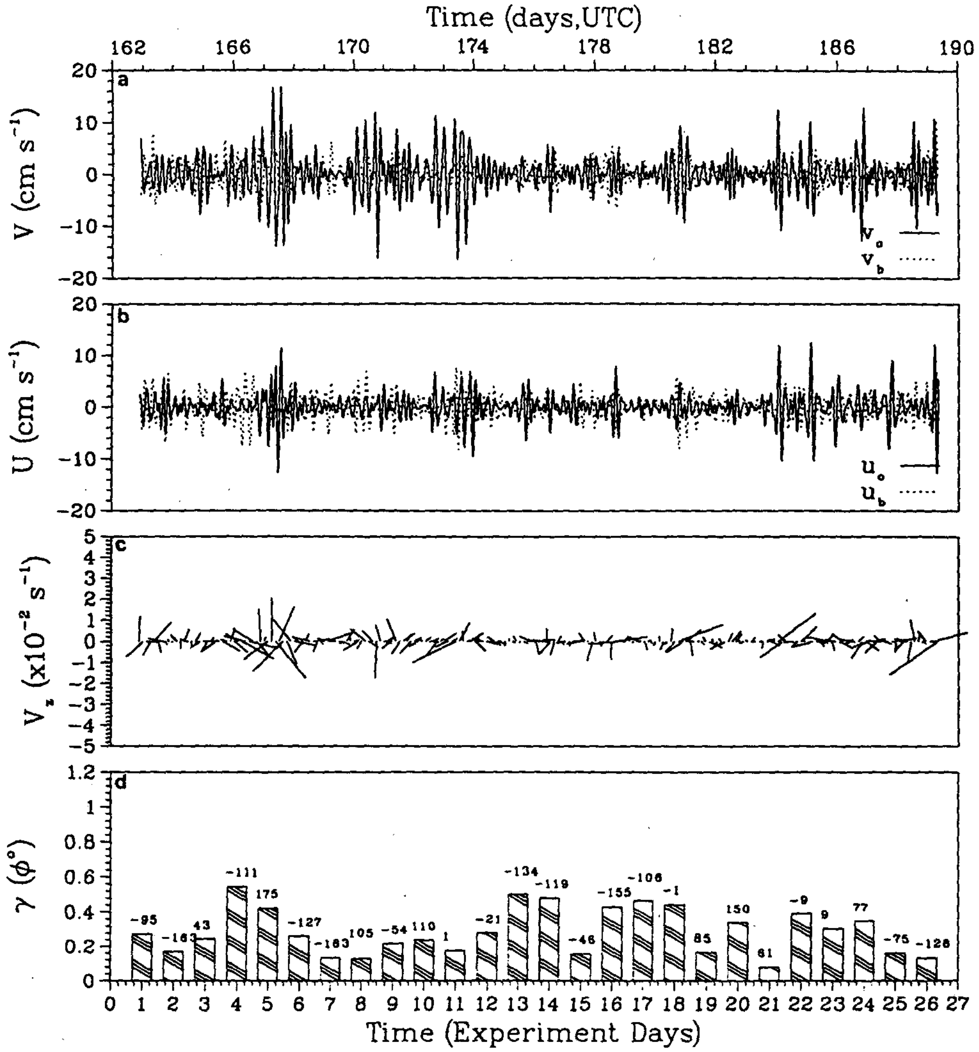

FIG. 13. Same as Fig. 8 except for detided, high-pass-filtered surface and subsurface current time series (V_{hf}) at D_E.

instrument performed well, providing observations 97% of the time over a large segment of the footprint (Shay et al. 1993). The data suggest complicated surface current regimes that were independently verified by shipboard measurements from the USNS *Bartlett* and the RV *Columbus Iselin* and research aircraft (NRL P-3, JPL, and NADC INSAR, and spotter plane) for several surface events. This consistency between the various observations, as a function of both space and time suggests the HF radar technique correctly observed surface currents. Thus, for the first time, the HF-radar-derived surface current data suggest a new *view* of mesoscale processes on a shelf forced by 3–5-day intrusions of the highly sheared baroclinic zone associated with the North Wall of the GS.

Given this highly complex regime, comparisons of the observed surface to subsurface currents at D_W and D_E indicated good correlations even though the subsurface currents were observed at 13.8 and 9.5 m beneath the surface. Mean biases were 2–4 cm s^{-1} and regression slopes were 0.8–1, implying that the surface currents were 10%–20% more than the subsurface values. These values were within the instrument error bounds cited by the manufacturer of 4 cm s^{-1}. Root-mean-square differences in the velocities ranged from 11 to 12 cm s^{-1} at D_W and 12 to 15 cm s^{-1} at D_E, which were consistently less than those found by Matthews et al. (1988). The histograms of the velocity differences ($u_o - u_b$, $v_o - v_b$) agreed with the theoretical Gaussian distribution as about 95% of the data were within ±1.96 times the standard deviation. Vertical current shears were $O(10^{-2}\ \mathrm{s}^{-1})$ over most of the time series and were also consistent with velocity profiles acquired in the vicinity of GS (Shay et al. 1994).

There were periods of high correlations ($\gamma > 0.8$) over the 27-day time series at D_W and D_E, which

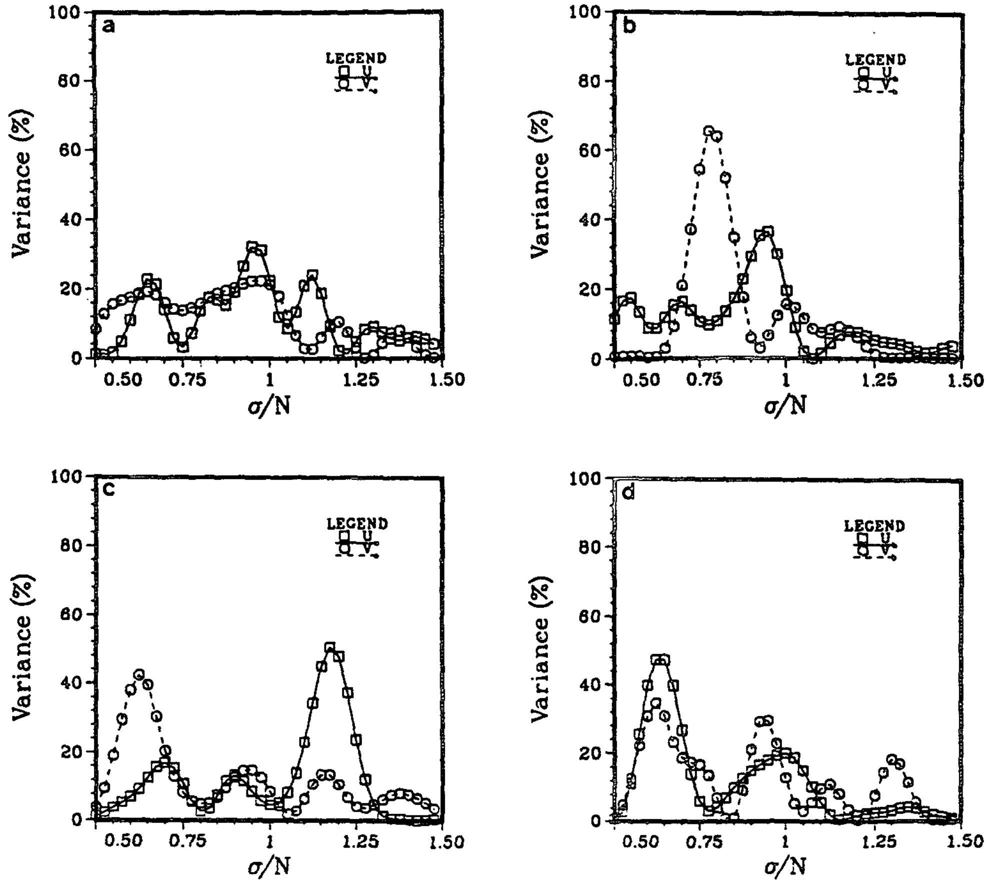

FIG. 14. High-frequency analysis for (a) D_W surface, (b) D_W subsurface, (c) D_E surface, and (d) D_E subsurface u (squares) and v (circles) components for the burst starting at 1800 UTC 15 June to 0600 UTC 17 June 1993. The ordinate represents explained variance (%) and the abscissa depicts frequency σ of the oscillations normalized by the frequency N of 3.8×10^{-4} s^{-1} (4.5 h).

were also consistent with those found from the five tracks of ADCP data acquired during the pilot experiment. It appears that higher-frequency wave motions (between f and N) vertically decorrelate ($\gamma < 0.5$) the surface and subsurface phenomena as these waves propagate along isopycnal surfaces. Higher-frequency motions (periods of 3–5 h) were also correlated to mean flow intrusions and possible scattering by the front itself. The divergence and convergence of these motions induces varying roughness on the sea surface that is detected by synthetic aperature radar measurements from aircraft- or satellite-based systems (Hughes and Gasparovic 1988). In addition, the tides explained between 8% and 24% of the observed current variability. Mean differences in the tidal amplitudes were 2–5 cm s^{-1} in the semidiurnal and diurnal tidal bands with a maximum difference of 7.7 cm s^{-1} in the K_1 constituents. In some instances, the tidal amplitudes were slightly larger than at the surface, which indicates internal tides excited by a barotropic tide propagating over a shelf break (i.e., Baines 1986). However, it must be emphasized that OSCR senses the surface currents in the upper half-meter ($\lambda/8\pi$) of the water column compared to 2, 5, or 10 m below the surface using conventional measurement techniques. While differences are expected because of the considerable vertical shears in this strong baroclinic frontal regime, understanding these surface current measurements and their relationship to upper ocean vertical shears and the vertical structure of currents and temperatures remains an important research goal.

Although the data acquisition from the HIRES-2 experiment was over a period of 27 days, the nearly continuous data have yielded a unique view of the kinematics and variability of surface currents. There is a broad spectrum of physical processes exciting surface current motions that can be resolved with time series at 700 points in an Eulerian context. Given the success of the OSCR system in the United Kingdom, the successful ONR pilot program in 1991 (Shay et al. 1992), and the 1993 HIRES experiment (Shay et al. 1993), it is envisioned that HF radar should play a key role in the design and execution of a national coastal oceanographic program (Brink et al. 1992; Smith and Brink 1994).

Acknowledgments. The authors gratefully acknowledge funding support by the Remote Sensing Program (Code 1121 RS) at the Office of Naval Research (N00014-91-J-4133) and the Minerals Management Service (Atlantic Coast Region) for the deployment and analysis of the OSCR data, and ONR support for the buoy measurements (N00014-91-J-1775). The National Park Service permitted us to use a part of the beach to set up the stations. Scientists on the USNS *Bartlett* and RV *Columbus Iselin* conducted high-resolution in situ sampling to ground truth the surface features from the OSCR maps. Aircraft missions organized by Chuck Luther (ONR) using a spotter plane confirmed surface features, and Dennis Trizna (NRL/ONR) made valuable suggestions to increase the signal to noise ratio. United States Coast Guard detachment at Oregon Inlet provided transportation of scientific and technical personnel to and from the research vessels. The Army Corps of Engineers facility at Duck, NC, provided two high-accuracy theodolites for the site survey. Lou Browning and Richard Marlin of the Frisco Fire Department kindly provided us with gadgets to irrigate the beach during the experiment. The authors are grateful for comments from our colleagues Don Olson, Richard Skop, and Claes Rooth, and from three anonymous reviewers that significantly improved the manuscript.

REFERENCES

Baines, P. G., 1986: Internal tides, internal waves and near-inertial motions. *Baroclinic Processes on Continental Shelves,* Christopher N. K. Mooers, Ed., American Geophysical Union, 19–31.

Barrick, D. E., 1980: Accuracy of parameter extraction from sample averaged sea echo Doppler spectra. *IEEE Trans. Antennas Propag.,* **28,** 1–11.

Brink, K. H., J. M. Bane, T. M. Church, C. W. Fairall, G. L. Geernaert, D. E. Hammond, S. M. Henrichs, C. S. Martens, C. A. Nittrouer, D. P. Rodgers, M. R. Roman, J. D. Roughgarden, R. L. Smith, L. D. Wright, and J. A. Yoder, 1992: Coastal ocean processes: A science prospectus. Woods Hole Oceanographic Institute, Tech. Rep. WHOI-92-18, Woods Hole, MA, 103 pp.

Brown, E. D., and W. B. Owens, 1981: Observations of the horizontal interactions between the internal wave field and mesoscale flow. *J. Phys. Oceanogr.,* **11,** 1474–1481.

Crombie, D. D., 1955: Doppler spectrum of sea echo at 13.56 Mc s^{-1}. *Nature,* **175,** 681–682.

Gonella, J., 1972: A rotary component method for analyzing meteorological and oceanographic time series. *Deep-Sea Res.,* **19,** 833–846.

Hammond, T. M., C. Pattiaratchi, D. Eccles, M. Osborne, L. Nash, and M. Collins, 1987: Ocean surface current radar (OSCR) vector measurements on the inner continental shelf. *Cont. Shelf Res.,* **7,** 411–431.

Herr, F., C. Luther, G. Marmorino, R. Mied, and D. Thompson, 1991: Science plan for the High Resolution Remote Sensing Program. *Eos,* **72,** 214.

Hughes, B. A., and R. F. Gasparovic, 1988: Introduction: Georgia Strait and SAR internal wave signatures. *J. Geophys. Res.,* **93**(10), 12 217–12 219.

Kundu, P. K., 1976: Ekman veering observed near the ocean bottom. *J. Phys. Oceanogr.,* **6,** 238–242.

Kunze, E., 1985: Near-inertial wave propagation in geostrophic shear. *J. Phys. Oceanogr.,* **15,** 544–565.

Lipa, B. J., and D. E. Barrick, 1983: Least-squares methods for the extraction of surface currents from CODAR crossed loop data: Application at ARSLOE. *IEEE J. Ocean Eng.,* **8**(4), 226–253.

Marmorino, G., and C. Trump, 1994: A salinity front and a current rip near Cape Hatteras, U.S.A. *J. Geophys. Res.,* **99,** 7627–7638.

Matthews, J. P., J. H. Simpson, and J. Brown, 1988: Remote sensing of the shelf sea currents using an HF radar system. *J. Geophys. Res.,* **93,** 2302–2310.

Minerals Management Service, 1991: North Carolina physical oceanography panel report. MMS 91-0011, U.S. Department of the Interior, Atlantic OCS Region, 45 pp.

Olbers, D. J., 1981: The propagation of internal waves in a geostrophic current. *J. Phys. Oceanogr.,* **11,** 1224–1233.

Osborne, M. J., 1991: OSCR and Interocean S4 current measurements in Poole Bay. *J. of Soc. Underwater Tech.,* **17**(1), 10–18.

Prandle, D., 1987: The fine-structure of nearshore tidal and residual circulations revealed by HF radar surface current measurements. *J. Phys. Oceanogr.,* **17,** 231–245.

——, 1991: A new view of near-shore dynamics based on HF radar. *Progress in Oceanography,* Vol. 27, Pergamon, 403–438.

——, and D. K. Ryder, 1989: Comparison of observed (HF radar) and modeled nearshore velocities. *Cont. Shelf Res.,* **9**(11), 941–963.

Ruddick, B. R., and T. M. Joyce, 1979: Observations of interactions between the internal wave field and low frequency flows in the North Atlantic. *J. Phys. Oceanogr.,* **9,** 498–517.

Shay, L. K., and R. L. Elsberry, 1987: Near-inertial ocean current response to hurricane Frederic. *J. Phys. Oceanogr.,* **17,** 1249–1269.

——, D. B. Ross, and H. C. Graber, 1992: Ocean surface current profiling using HF radar. RSMAS Tech. Rep. TR 92-004, Rosenstiel School of Marine and Atmospheric Science, University of Miami, Miami, FL, 55 pp.

——, H. C. Graber, D. B. Ross, L. Chemi, N. Peters, J. Hargrove, R. Vakkayil, and L. Chamberlain, 1993: Measurements of ocean surface currents using an HF radar during HIRES-2. RSMAS Tech. Rep. TR 93-007, Rosenstiel School of Marine and Atmospheric Science, University of Miami, Miami, FL, 66 pp.

——, E. J. Walsh, and P. C. Zhang, 1994: Orbital velocities induced by surface waves. *J. Atmos. Oceanic Technol.,* **11,** 1117–1125.

Smith, R. L., and K. H. Brink, 1994: Coastal ocean processes: Wind-driven transport processes on the U.S. West Coast. Coop Report 4, Woods Hole Oceanographic Institute Tech. Rept. WHOI-94-20, Woods Hole, MA, 140 pp.

Stewart, R. H., and J. W. Joy, 1974: HF radio measurements of surface currents. *Deep-Sea Res.,* **21,** 1039–1049.

Wesson, J. C., and M. C. Gregg, 1994: Mixing at the Camarinal Sill in the Strait of Gibraltar. *J. Geophys. Res.,* **99,** 9847–9878.